

# Differential cross sections for muonic atom scattering in solid hydrogenic targets

Andrzej Adamczak\*

*Institute of Nuclear Physics, Polish Academy of Sciences, PL-31342 Kraków, Poland  
and Rzeszów Technical University, PL-35959 Rzeszów, Poland*

(Dated: August 23, 2021)

## Abstract

The differential cross sections for low-energy muonic hydrogen atom scattering in solid molecular  $H_2$ ,  $D_2$  and  $T_2$  targets under low pressure have been calculated for various temperatures. The polycrystalline fcc and hcp structure of the solid hydrogenic targets are considered. The Bragg and phonon scattering processes are described using the Debye model of a solid. The calculated cross sections are used for Monte Carlo simulations of the muonic atom slowing down in these targets. They have been successfully applied for a description of the production of the muonic atom beams in the multilayer hydrogenic crystals.

PACS numbers: 34.50.-s, 36.10.Dr

arXiv:0801.0138v1 [physics.atom-ph] 30 Dec 2007

---

\*Electronic address: andrzej.adamczak@ifj.edu.pl

## I. INTRODUCTION

The aim of this paper is to calculate the differential cross for muonic hydrogen atom scattering in low-pressure molecular hydrogenic crystals and to study the muonic atom deceleration in such crystals. The solid hydrogenic targets have been used for the production of the muonic hydrogen atom beams, which have been applied to the time-of-flight measurements of various muonic-atom and muonic-molecular processes (see e.g., Refs. [1, 2, 3, 4, 5, 6]). The bulk hydrogenic crystals are employed in the investigations of muon-catalyzed fusion of the hydrogen isotopes at high target densities and for various populations of the rotational molecular levels [7, 8, 9, 10, 11, 12, 13]. Hydrogenic solid targets are also used in a novel method of spectroscopy of the radioactive muonic atoms [14, 15].

Monte Carlo simulations of such experiments, which used the perfect-gas model of a target and the available differential cross sections [16, 17] for the muonic atom scattering from hydrogen-isotope nuclei, did not reproduce the experimental low-energy ( $\lesssim 1$  eV) data. Moreover, even the use of the cross sections for scattering from isolated hydrogenic molecules [18, 19] did not lead to an agreement between theory and experiment [1, 8]. Thus, it is necessary to take into account condensed-state effects of the muonic atom scattering in the solids. In particular, interpreting the experimental data and planning new experiments demand the knowledge of the differential cross sections for scattering in the hydrogenic crystals.

A few examples of the total cross sections for  $p\mu$  and  $d\mu$  atom scattering in solid  $H_2$  and  $D_2$  at a fixed target temperature  $T = 3$  K were shown in Ref. [20]. Below, a method of calculation of the partial differential cross sections for muonic hydrogen atom scattering in the polycrystalline hydrogenic targets at various temperatures is presented in detail. These cross sections are evaluated using the amplitudes for muonic atom scattering from isolated hydrogenic molecules [19] and the Van Hove response function  $\mathcal{S}$  [21]. The isotropic Debye model of the solid is employed.

In Sec. II, the coherent and incoherent cross sections for the scattering in hydrogenic crystals are expressed by the scattering amplitudes calculated for the isolated molecules. The incoherent cross section, which includes the elastic scattering, incoherent phonon scattering, and rotational-vibrational transitions in the target molecules is discussed in Sec. III. The Bragg scattering for the fcc and hcp structures, which are observed in hydrogenic crystals, is considered in Sec. IV. The inelastic coherent cross section, which leads to the creation or annihilation of one phonon in a muonic atom collision with the crystal is calculated in Sec. V. Some examples of the calculated cross sections for the homogeneous hydrogenic targets at various temperatures are shown in Sec. VI. Most examples are given for the so-called “normal” [22] targets  $nH_2$ ,  $nD_2$ , and  $nT_2$ , which are characterized by the statistical distribution of the molecular rotational levels  $K = 0$  and 1.

Symmetry of the wave function of a homonuclear hydrogenic molecule is definite. In the hydrogen case, the total nuclear spin  $I$  of  $H_2$  equals 0 or 1. The singlet spin state  $I = 0$  is asymmetric. As a result, only the symmetric spatial wave functions with even values of the rotational number  $K$  are allowed. The  $H_2$  molecules in such states are called parahydrogen molecules. For the symmetric triplet state  $I = 1$ , only odd values of  $K$  can occur. This defines the orthohydrogen molecules. The situation is similar for the  $T_2$  molecules, since the spin  $s$  of proton or triton is equal to 1/2. In the deuterium case, one has  $s = 1$ . The total two-deuteron wave function must be symmetric. For the symmetric spin states  $I = 0, 2$ , the spatial wave function is symmetric, which corresponds to even  $K$ .

The  $D_2$  molecules in such states are called orthodeuterium molecules. The paradeuterium molecules are characterized by  $I = 1$  and odd  $K$ . The ortho and parastates of the hydrogenic molecules are remarkably stable, in the absence of a catalyst [22]. As a result, during rapid cooling of the equilibrated  $nH_2$ ,  $nD_2$ , or  $nT_2$  gas, the even- $K$  states deexcite to  $K = 0$  and the odd- $K$  states deexcite to  $K = 1$ . The ortho-para transitions can occur in certain collisions with muonic hydrogen atoms. This is possible if the muonic atom interaction with a homonuclear molecule is spin-dependent. Such a situation takes place when the hydrogen isotope in the impinging atom is identical with those in the homonuclear target molecule, e.g., in the  $p\mu + H_2$  scattering [16, 17]. In this case, the exchange forces between the three identical nuclei should be taken into account. In particular, they lead to a high probability of the muon exchange between two nuclei taking part in direct collision. When the spin projections of these nuclei are opposite, the nuclear spin  $I$  of the target molecule can change in the collision process. As a result, the simultaneous rotational ortho-para transition takes place. Such spin effects are included in the presented calculations.

The obtained differential cross sections are used for Monte Carlo simulations of the muonic atom deceleration. Some results of these simulations are presented in Sec. VII.

## II. COHERENT AND INCOHERENT CROSS SECTIONS

A muonic hydrogen atom  $a\mu$  can be approximately treated as a small neutron-like particle. Therefore, the methods derived for the description of neutron scattering in condensed matter can be applied to  $a\mu$  scattering in dense hydrogenic targets. Below, the Van Hove formalism [21] is adapted to the calculation of the differential cross sections for  $a\mu$  scattering in the hydrogenic crystals. In this formalism, the cross sections are expressed in terms of the response function  $\mathcal{S}$ , which depends solely on properties of a given target for fixed momentum and energy transfers. A definition of this function involves both quantum-mechanical and statistical averaging over the target states at temperature  $T$ .

It is assumed that there is no coupling between the translational and collective motions of the molecules in the condensed target and the molecular rotations and vibrations. The internal molecular degrees of freedom are already included in a single-molecule process [19] and, therefore, do not enter into the response function. It is assumed that a bulk dense target is kept at a sufficiently low pressure, so that distortions of a single bound molecule due to the interactions with neighbors can be neglected. This assumption is fulfilled in the case of low-pressure ( $\ll 10$  kbar) solid hydrogenic targets [22, 23]. The mean distance between the neighboring molecules in such targets is several times greater than the diameter of these molecules. The Van der Waals force between the molecules is weak. As a result, the rotational and vibrational numbers remain good quantum numbers, although small broadening of certain excited molecular levels takes place [24]. This broadening is not taken into account in the presented calculations.

Low-pressure hydrogenic solids are quantum molecular crystals, which are characterized by a large amplitude of the zero-point vibrations of the molecules in the lattice. The standard lattice dynamics can be applied to these crystals, after certain renormalization of the molecule-interaction potential [22, 23]. Also, the Debye model of a solid can be used as a reasonable approximation.

The wavelength of a very slow ( $\lesssim 10$  meV) muonic hydrogen atom is comparable to the nearest-molecule distance of about  $3.5 \text{ \AA}$  [22, 23]. Therefore, strong interference effects can be observed at such energies. These effects are described using a conventional separation of

the total differential cross sections on the incoherent and coherent fractions. The coherent scattering takes place only if specific geometrical conditions are fulfilled. Analogous to the neutron coherent scattering [25], the coherent cross section for  $a\mu$  scattering in a solid single-isotope hydrogenic target can be written down in the form:

$$\left(\frac{\partial^2\sigma}{\partial\Omega\partial\varepsilon'}\right)_{\text{coh}} = N_{\text{mol}} \frac{k'}{k} \sigma_{\text{coh}} \mathcal{S}(\boldsymbol{\kappa}, \omega), \quad (1)$$

where  $N_{\text{mol}}$  is the number of molecules in the target. The energy transfer  $\omega$  and the momentum transfer  $\boldsymbol{\kappa}$  to the lattice are, respectively, equal to

$$\omega = \varepsilon - \varepsilon' - \Delta E, \quad \boldsymbol{\kappa} = \mathbf{k} - \mathbf{k}', \quad (2)$$

where  $\varepsilon$  and  $\varepsilon'$  denote the initial and final kinetic energies of the scattered muonic atom and  $\Delta E$  is the sum of the internal-energy changes of  $a\mu$  and of the target molecules. Vectors  $\mathbf{k}$  and  $\mathbf{k}'$  stand for the initial and final momenta of  $a\mu$ . These momenta and collision energies are connected by the relations

$$\varepsilon = \frac{1}{2}k^2/M_{a\mu}, \quad \varepsilon' = \frac{1}{2}k'^2/M_{a\mu}, \quad (3)$$

in which  $M_{a\mu}$  denotes the  $a\mu$  mass. The function  $\sigma_{\text{coh}}$  in Eq. (1) is expressed by the amplitude  $\mathcal{F}^{\text{mol}}$  for  $a\mu$  scattering from an isolated molecule [19]

$$\sigma_{\text{coh}} = \overline{|\mathcal{F}^{\text{mol}}|^2}. \quad (4)$$

The horizontal bar stands here for averaging over a random distribution of the total spin  $\mathcal{J}$  of the  $a\mu$ +molecule system and over a distribution of the initial rotational states of the molecules. It is assumed that there is no correlation between the direction of the molecular spin  $\mathbf{I}$  and the lattice site.

Incoherent scattering does not include interference effects from different molecules in the lattice. The incoherent cross section takes a general form [25]

$$\left(\frac{\partial^2\sigma}{\partial\Omega\partial\varepsilon'}\right)_{\text{inc}} = N_{\text{mol}} \frac{k'}{k} \sigma_{\text{inc}} \mathcal{S}_i(\boldsymbol{\kappa}, \omega), \quad (5)$$

where

$$\sigma_{\text{inc}} = \overline{|\mathcal{F}^{\text{mol}}|^2} - \overline{|\mathcal{F}^{\text{mol}}|^2}, \quad (6)$$

and the incoherent response function  $\mathcal{S}_i(\boldsymbol{\kappa}, \omega)$  is a fraction of the total response function  $\mathcal{S}(\boldsymbol{\kappa}, \omega)$ . In the limit of large momentum transfers, the coherent processes disappear, so that  $\mathcal{S}(\boldsymbol{\kappa}, \omega) \approx \mathcal{S}_i(\boldsymbol{\kappa}, \omega)$ . The total differential cross section  $\partial^2\sigma/\partial\Omega\partial\varepsilon'$  is a sum of the coherent (1) and incoherent (5) cross sections.

The inelastic scattering processes which change the internal state of  $a\mu$  or that of the target molecule (such as the spin-flip and isotopic-exchange reactions and the rotational-vibrational transitions) are fully incoherent processes. No averaging over the states of the different target molecules is performed and, therefore, in this case  $\sigma_{\text{inc}}$  reduces to the single-molecule squared amplitude

$$\sigma_{\text{inc}} = |\mathcal{F}^{\text{mol}}|^2 \quad \text{and} \quad \sigma_{\text{coh}} = 0.$$

When the states of the muonic atom and molecule are not changed during collision,  $\sigma_{\text{coh}}$  and  $\sigma_{\text{inc}}$  are equal to the coherent and incoherent fractions of the elastic cross section for  $a\mu$  scattering from a single molecule. Their values depend on a given choice of the hydrogen isotopes, the total spin  $F$  of  $a\mu$ , the population of the molecular rotational levels, and the collision energy. In particular, when  $\mathcal{F}^{\text{mol}}$  does not depend on the spin  $\mathcal{J}$  and only one rotational state is populated, the scattering is fully coherent

$$\sigma_{\text{coh}} = \left| \overline{\mathcal{F}^{\text{mol}}} \right|^2 = \overline{|\mathcal{F}^{\text{mol}}|^2} \quad \text{and} \quad \sigma_{\text{inc}} = 0.$$

For example, such a situation takes place in the case of elastic scattering  $d\mu + \text{H}_2$  in the ground rotational state  $K = 0$  of the  $\text{H}_2$  molecule.

In general, both  $\sigma_{\text{coh}}$  and  $\sigma_{\text{inc}}$  can have nonzero values. In Table I, these functions are shown in the limit  $\varepsilon \rightarrow 0$ , for the cases  $p\mu + \text{H}_2$ ,  $t\mu + \text{T}_2$ , and  $d\mu + \text{D}_2$  and for several values of  $F$  and  $K$ .

TABLE I: Coherent  $\sigma_{\text{coh}}$  and incoherent  $\sigma_{\text{inc}}$  elastic cross sections (in  $10^{-20}$   $\text{cm}^2/\text{sr}$ ) for a single hydrogenic molecule, at the collision energy  $\varepsilon \rightarrow 0$ .

process	$F$	$K$	$\sigma_{\text{coh}}$	$\sigma_{\text{inc}}$
$p\mu + \text{H}_2$	0	0	88.5	0.0
	0	1	88.7	0.0
	1	0	126.2	0.0
	1	1	124.8	87.6
$t\mu + \text{T}_2$	0	0	325.7	0.0
	0	1	324.9	0.0
	1	0	342.9	0.0
	1	1	342.4	10.5
$d\mu + \text{D}_2$	1/2	0	64.7	0.15
	1/2	1	64.4	0.06
	3/2	0	64.5	0.38
	3/2	1	64.3	0.15

### III. INCOHERENT SCATTERING

The incoherent response function  $\mathcal{S}_i$  can be rigorously calculated for harmonic crystals [21, 26]. Using the so-called phonon expansion of  $\mathcal{S}_i$  for a cubic Bravais lattice (one molecule per lattice cell), the incoherent cross section (5) takes the form:

$$\begin{aligned} \left( \frac{\partial^2 \sigma}{\partial \Omega \partial \varepsilon'} \right)_{\text{incoh}} &= N_{\text{mol}} \frac{k'}{k} \sigma_{\text{inc}} \exp(-2W) \\ &\times \left[ \delta(\omega) + \sum_{n=1}^{\infty} g_n(\omega) \frac{(2W)^n}{n!} \right], \end{aligned} \quad (7)$$

where  $\exp(-2W)$  denotes the Debye-Waller factor, which is familiar in the theory of neutron scattering. This expansion is also a fair approximation for any cubic lattice, e.g., the fcc structure. The exponent of the Debye-Waller factor is by definition equal to

$$2W(\boldsymbol{\kappa}) \equiv \langle (\boldsymbol{\kappa} \cdot \mathbf{u})^2 \rangle_T, \quad (8)$$

in which  $\mathbf{u}$  is the displacement of the molecule from its lattice site and  $\langle \dots \rangle_T$  denotes the quantum-mechanical and statistical averaging at temperature  $T$ . In particular, for a cubic-crystal structure

$$2W = \frac{1}{3} \langle \mathbf{u}^2 \rangle_T \kappa^2. \quad (9)$$

It follows from (8) that  $2W$  does not disappear at  $T = 0$  because the mean square displacement tends in this limit to a finite value determined by the zero-point vibrations of the molecule in the lattice. The functions  $g_n$  in Eq. (7) are defined as

$$\begin{aligned} g_1(w) &= \frac{1}{2W} \frac{\kappa^2}{2M_{\text{mol}}} \frac{Z(w)}{w} [n_{\text{B}}(w) + 1], \\ g_n(w) &= \int_{-\infty}^{\infty} dw' g_1(w - w') g_{n-1}(w'), \\ \int_{-\infty}^{\infty} dw g_n(w) &= 1, \end{aligned} \quad (10)$$

where  $M_{\text{mol}}$  is the mass of the molecule. The normalized density of vibrational states  $Z(w)$  in the isotropic Debye model has the following form:

$$Z(w) \equiv \begin{cases} 3w^2/w_{\text{D}}^3 & \text{if } w \leq w_{\text{D}} \\ 0 & \text{if } w > w_{\text{D}}, \end{cases} \quad (11)$$

where  $w_{\text{D}} = k_{\text{B}}\Theta_{\text{D}}$  is the Debye energy corresponding to the Debye temperature  $\Theta_{\text{D}}$  ( $k_{\text{B}}$  stands for the Boltzmann constant). For the low-pressure hydrogenic crystals,  $\Theta_{\text{D}}$  is on the order of 100 K. Although differences between the masses of the hydrogen isotopes are quite large, isotopic effects in  $\Theta_{\text{D}}$  for these crystals are quite small, due to quantum effects [22, 23]. The function  $n_{\text{B}}(w)$  in Eqs. (10) denotes the Bose factor

$$n_{\text{B}}(w) = [\exp(w/k_{\text{B}}T) - 1]^{-1}, \quad (12)$$

which determines the phonon population at a given  $T$ .

Note that there is no momentum-conservation condition in the incoherent cross section (7). The  $\delta$  function in Eq. (7) represents the recoil-less scattering from the rigid lattice. In the case of elastic scattering ( $\Delta E = 0$ ),  $a\mu$  cannot change its energy in this process. This is connected with a large mass of the solid target. The next terms give broad distributions corresponding to the subsequent multiphonon processes. In particular, the term with  $n = 1$  describes incoherent  $a\mu$  scattering with simultaneous creation or annihilation of one phonon. The amplitudes of all the processes are proportional to the Debye-Waller factor, which decreases with the rising momentum transfer.

Elastic  $a\mu$  scattering from a free molecule is described by a single function. In a solid, this function is replaced by a set of functions corresponding to the strictly elastic and multiphonon processes which are proportional to  $\kappa^{2n}$ . The same conclusion can be drawn

for any incoherent process, e.g., for a rotational excitation of the target molecule. In such a scattering event, the nonphonon cross section is connected with the energy transfer  $\Delta E$  to the molecule. The higher energy transfers are due to the rotational excitation with simultaneous phonon creation.

When the momentum transfer is small ( $2W \ll 1$ ), only the several lowest terms in Eq. (7) are important. On the other hand, in the limit  $2W \gg 1$  (weak binding), many multiphonon terms give comparable contributions to the cross section. For sufficiently large  $\kappa^2$ , it is convenient to use the impulse approximation in which  $\mathcal{S}_i$  takes a general Gaussian form for any target described by a time-independent Hamiltonian [27]. In this approach, the incoherent cross section is equal to

$$\left( \frac{\partial^2 \sigma}{\partial \Omega \partial \varepsilon'} \right)_{\text{inc}} = N_{\text{mol}} \frac{k'}{k} \sigma_{\text{inc}} \times \frac{1}{\Delta_{\text{R}} \sqrt{\pi}} \exp \left[ - \left( \frac{\omega - \omega_{\text{R}}}{\Delta_{\text{R}}} \right)^2 \right], \quad (13)$$

where

$$\Delta_{\text{R}} = \sqrt{8 \mathcal{E}_T \omega_{\text{R}} / 3} \quad (14)$$

is the Doppler width of the asymptotic form of  $\mathcal{S}_i$ . The mean kinetic energy of a single molecule in the lattice at temperature  $T$  is denoted by  $\mathcal{E}_T$  and  $\omega_{\text{R}}$  is the recoil energy

$$\omega_{\text{R}} = \frac{1}{2} \kappa^2 / M_{\text{mol}}. \quad (15)$$

For a harmonic solid

$$\mathcal{E}_T = \frac{3}{2} \int_0^\infty dw Z(w) w \left[ n_{\text{B}}(w) + \frac{1}{2} \right]. \quad (16)$$

This energy contains a contribution from the zero-point vibrations of the lattice molecules. In the case of low-pressure hydrogenic crystal, one has  $T/\Theta_{\text{D}} \ll 1$ . In this limit,  $\mathcal{E}_T$  and the effective target temperature  $T_{\text{eff}}$

$$T_{\text{eff}} = \frac{2}{3} \mathcal{E}_T / k_{\text{B}}. \quad (17)$$

are well approximated by

$$\mathcal{E}_T = \frac{9}{16} w_{\text{D}}, \quad \text{and} \quad T_{\text{eff}} = \frac{3}{8} \Theta_{\text{D}}, \quad (18)$$

respectively. In particular, for a 3-K zero-pressure solid deuterium target with  $\Theta_{\text{D}} = 108$  K, one obtains  $\mathcal{E}_T = 5.2$  meV and  $T_{\text{eff}} \approx 40$  K. Thus,  $T_{\text{eff}} \gg T$ , which means that the cross sections calculated for 3-K perfect-gas  $\text{D}_2$  should not be used for a description of the solid  $\text{D}_2$  target at the same temperature. Relatively high values of  $\mathcal{E}_T$  in the solid  $\text{H}_2$  and  $\text{D}_2$  targets have been experimentally confirmed using deep inelastic neutron scattering [28, 29, 30].

At very high collision energies  $\varepsilon \gg w_{\text{D}}$  and  $\varepsilon \gg \Delta E$ , the approximation  $\varepsilon' \approx \varepsilon$  ( $k' \approx k$ ) is valid. As a result, the cross section (13) averaged over  $\varepsilon'$  tends to the static approximation

$$\left( \frac{d\sigma}{d\Omega} \right)_{\text{inc}} = N_{\text{mol}} \sigma_{\text{inc}}. \quad (19)$$

This cross section no longer depends on the target structure and is equal to the sum of the free-molecule incoherent cross sections. Since, at high energies, coherent effects disappear, the total differential cross section  $d\sigma/d\Omega$  is given by Eq. (19) with  $\sigma_{\text{inc}}$  replaced by  $|\mathcal{F}^{\text{mol}}|^2$ .

The influence of the lattice binding on the incoherent scattering is described by the following function:

$$\mathcal{C}_{\text{inc}} \equiv \frac{1}{4\pi N_{\text{mol}}} \left( \frac{M_{a\mu}}{\mathcal{M}} \right)^2 \int d\Omega d\varepsilon' \left( \frac{\partial^2 \sigma}{\partial \Omega \partial \varepsilon'} \right)_{\text{inc}}, \quad (20)$$

where  $\mathcal{M}$  denotes the reduced mass of the  $a\mu$ +molecule system. It is assumed here that  $\mathcal{F}^{\text{mol}}$  is constant. The function  $\mathcal{C}_{\text{inc}}$  for elastic ( $\Delta E = 0$ )  $p\mu$  scattering in 3-K solid H<sub>2</sub> at zero pressure is presented in Fig. 1. The different curves show contributions from the nonphonon,

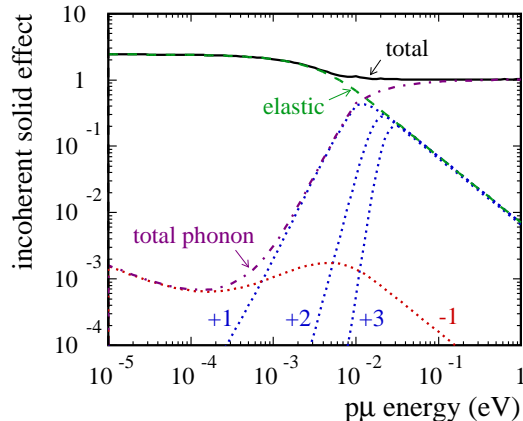


FIG. 1: (Color online) Function  $\mathcal{C}_{\text{inc}}$  versus energy  $\varepsilon$  for incoherent elastic scattering of  $p\mu$ -atom in 3-K solid-hydrogen. Subsequent phonon-creation processes are denoted by “+1” (one-phonon), “+2” (two-phonon), and “+3” (three-phonon). Label “-1” stands for annihilation of one phonon.

phonon creation, and phonon annihilation processes. Every single process falls exponentially for sufficiently large energies, which is due to the Debye-Waller factor in Eq. (7). At energies below a few meV, the nonphonon elastic scattering is dominant. The phonon annihilation, which is strongly suppressed by the Bose factor at 3 K, prevails over the phonon creation only at  $\varepsilon \lesssim 0.7$  meV. The subsequent phonon-creation processes appear when  $\varepsilon$  rises. Finally, they dominate the scattering at  $\varepsilon \gg w_{\text{D}}$ , where the static-approximation limit is reached and  $\mathcal{C}_{\text{inc}} = 1$ . For  $\varepsilon \rightarrow 0$ , one has  $\mathcal{C}_{\text{inc}} = (M_{a\mu}/\mathcal{M})^2 = 2.24$ . In Fig. 2, contributions of the nonphonon and phonon fractions of  $\mathcal{S}_i$  to the total cross section are plotted for the rotational deexcitation  $K = 1 \rightarrow 0$  of a D<sub>2</sub> molecule bound in 3-K solid deuterium, in collision with a  $d\mu(F = 3/2)$  atom. The cross section is proportional to  $\varepsilon^{-1/2}$  at  $\varepsilon \rightarrow 0$ . Even at the lowest energies, the phonon processes are more important than in the elastic case (cf. Fig. 1) because the rotational energy release of 7.5 meV is comparable to  $w_{\text{D}} \approx 9$  meV.

#### IV. COHERENT ELASTIC SCATTERING

The fraction of the response function  $\mathcal{S}$  that describes coherent elastic scattering (Bragg scattering) is well known in the neutron theory (see e.g., Ref. [25]). When applied to Eq. (1), it leads to the following coherent elastic cross section for a perfect-crystal lattice with  $N_d$



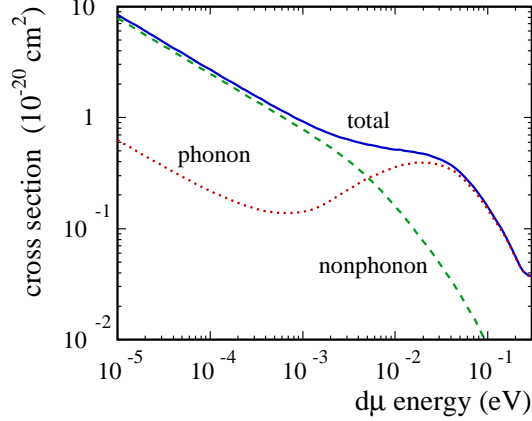


FIG. 2: (Color online) Phonon and nonphonon contributions to the cross section for the rotational deexcitation  $d\mu(F = 3/2) + D_2(K = 1) \rightarrow d\mu(F = 3/2) + D_2(K = 0)$  in solid deuterium at  $T = 3$  K.

identical molecules per unit cell of volume  $V_0$ :

$$\left(\frac{d\sigma}{d\Omega}\right)_{\text{coh}}^{\text{el}} = N \frac{(2\pi)^3}{V_0} \sum_{\boldsymbol{\tau}} |F_N(\boldsymbol{\tau})|^2 \times \delta(\boldsymbol{\kappa} - \boldsymbol{\tau}) \exp[-2W(\kappa^2)], \quad (21)$$

$F_N(\boldsymbol{\tau})$  being the unit-cell structure factor

$$|F_N(\boldsymbol{\tau})|^2 = \sigma_{\text{coh}} \left| \sum_{d=1}^{N_d} \exp(i\boldsymbol{\tau} \cdot \mathbf{d}) \right|^2. \quad (22)$$

The summation in Eq. (21) is performed over the reciprocal-lattice vectors  $\boldsymbol{\tau}$ . The vector  $\mathbf{d}$  denotes the position of a given molecule in the unit cell and  $N$  is the number of the unit cells in the crystal. The Bragg scattering of  $a\mu$  in a large crystal is possible only when the momentum transfer is equal to one of the reciprocal lattice vectors

$$\boldsymbol{\kappa} = \mathbf{k} - \mathbf{k}' = \boldsymbol{\tau}. \quad (23)$$

The intensity of scattering peaks is determined by the Debye-Waller factor and by the value of  $\sigma_{\text{coh}}$  for the specific momentum  $k$  and the scattering angle  $\vartheta$ . At high energies, the elastic Bragg scattering vanishes. Below the Bragg cutoff energy

$$\varepsilon_B = \frac{1}{8} \tau_{\text{min}}^2 / M_{a\mu}, \quad (24)$$

the condition (23) cannot possibly be fulfilled and the elastic coherent scattering disappears. The value of the shortest nonzero vector  $\boldsymbol{\tau}$  is denoted here by  $\tau_{\text{min}}$ .

The Bragg-cutoff energies for various combinations of the muonic atoms and hydrogenic targets are shown in Table II, for the 3-K fcc targets at zero-pressure. They have been calculated using the hydrogenic-crystal data from Refs. [22, 23].

TABLE II: The Bragg cutoff energy  $\varepsilon_B$  (in meV) for  $p\mu$ ,  $d\mu$ , and  $t\mu$  atom scattering in the 3-K fcc crystals of  $n\text{H}_2$ ,  $n\text{D}_2$ , and  $n\text{T}_2$  at zero pressure.

lattice	$n\text{H}_2$	$n\text{D}_2$	$n\text{T}_2$
$p\mu$	1.94	2.13	2.21
$d\mu$	1.02	1.12	1.17
$t\mu$	0.69	0.76	0.79

When scattering takes place from a polycrystalline sample, which is usually the case in the muonic-hydrogen physics, Eq. (21) can be averaged over all orientations of the lattice. This gives the following cross section:

$$\left(\frac{d\sigma}{d\Omega}\right)_{\text{coh}}^{\text{el}} = N \frac{2\pi^2}{V_0} \frac{1}{k^2} \sum_{\boldsymbol{\tau}} |F_N(\boldsymbol{\tau})|^2 \frac{1}{\tau} \times \delta\left(1 - \frac{\tau^2}{2k^2} - \cos\vartheta\right) \exp[-2W(\kappa^2)]. \quad (25)$$

The scattering now takes place in the Debye-Scherrer cones around the direction of  $\mathbf{k}$ . The cones have the semi-angles  $\vartheta$  subject to the condition  $\cos\vartheta = 1 - \tau^2/2k^2$ . In Fig. 3,  $\vartheta$  is

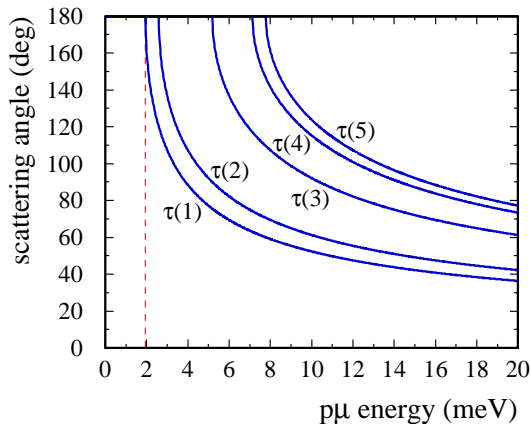


FIG. 3: (Color online) Scattering angle  $\vartheta$  in Bragg scattering of  $p\mu$  in 3-K  $n\text{H}_2$  versus the collision energy and the value of the reciprocal-lattice vector  $\boldsymbol{\tau}$ . The fcc polycrystalline structure of the target is assumed.

plotted as a function of the  $p\mu$  kinetic energy in a 3-K  $n\text{H}_2$  target with the polycrystalline fcc structure. The scattering angle is shown for the five smallest values  $\tau(i)$ ,  $i = 1, \dots, 5$  of the vectors  $\boldsymbol{\tau}$ . As one can see from Eq. (25) and Fig. 3, the subsequent Bragg peaks appear at  $\vartheta = 180^\circ$ . When  $\varepsilon$  increases, this backward scattering opens into a cone which moves continuously towards the forward direction. The total cross section  $\sigma_{\text{coh}}^{\text{el}}(\tau)$  is expressed by the formula

$$\sigma_{\text{coh}}^{\text{el}} = N \frac{4\pi^3}{V_0} \frac{1}{k^2} \sum_{\boldsymbol{\tau}}^{\tau < 2k} |F_{\boldsymbol{\tau}}|^2 \frac{1}{\tau} \exp[-2W(\tau^2)]. \quad (26)$$

where  $z(\tau)$  is the number of  $\tau$ -vectors with the same magnitude  $\tau$  and  $|F_\tau|^2$  denotes the average value of  $|F_N(\boldsymbol{\tau})|^2$  for just these vectors.

In order to illustrate the energy dependence of interference effects, the function

$$\mathcal{C}_{\text{Bragg}}(\varepsilon) \equiv \frac{4\pi^3}{V_0} \frac{|F_\tau|^2}{N_d \sigma_{\text{coh}}} \frac{1}{k^2} \sum_{\tau < 2k} \frac{1}{\tau}, \quad (27)$$

is plotted in Fig. 4 for  $p\mu$  scattering in polycrystalline  $n\text{H}_2$  with the fcc and hcp structures. This function is equal to the total Bragg cross section for scattering in a rigid lattice [ $\exp(-2W) \equiv 1$ ], calculated per one molecule. It is assumed that  $\sigma_{\text{coh}}$  is constant. The

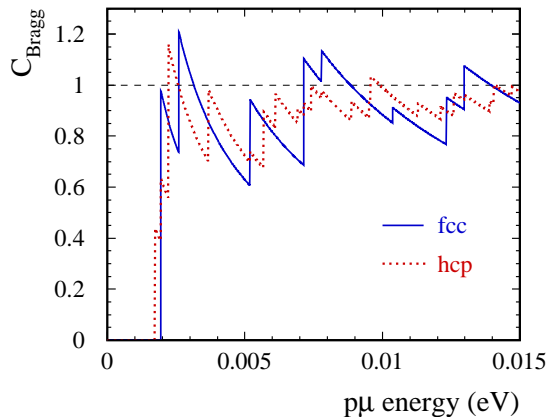


FIG. 4: (Color online) The Bragg pattern in the case of scattering of a  $p\mu$  atom in a 3-K polycrystalline  $n\text{H}_2$  target with the fcc and hcp structures.

coherent scattering is forbidden below  $\varepsilon_B \approx 2$  meV. The subsequent Bragg peaks appear for the rising  $p\mu$  energy. The Bragg-cutoff energy is slightly lower for the hcp structure.

## V. COHERENT INELASTIC SCATTERING

The inelastic coherent scattering is connected with the energy transfer between  $a\mu$  and the collective degrees of freedom of the target. Such a scattering describes the coherent annihilation and creation of phonons, but it does not include changes of the internal state of the target molecule ( $\Delta E = 0$ ). Thus, the energy transfer to the lattice is  $\omega = \varepsilon - \varepsilon'$ . The inelastic coherent cross section for  $a\mu$  scattering in a hydrogenic solid can be calculated using the methods developed for the coherent scattering of neutrons [25]. In this paper, coherent effects are taken into account only in the most important one-phonon processes. An estimation of the multiphonon cross sections is much more difficult. Therefore, these cross sections are calculated in the incoherent approximation. In the case of a Bravais

harmonic lattice, the coherent one-phonon cross section is given by the following formula:

$$\begin{aligned}
\left(\frac{\partial^2 \sigma}{\partial \Omega \partial \varepsilon'}\right)_{\text{coh},1}^{\text{inel}} &= \frac{k'}{k} \frac{(2\pi)^3}{V_0} \frac{1}{2M_{\text{mol}}} \sum_{\boldsymbol{\tau}} \sigma_{\text{coh}} \\
&\times \exp[-2W(\boldsymbol{\kappa})] \sum_{j,\mathbf{q}} \frac{|\boldsymbol{\kappa} \cdot \boldsymbol{\sigma}^j|^2}{w_j} \\
&\times \left[ n_{\text{B}}^j(\mathbf{q}) \delta(\omega + w_j) \delta(\boldsymbol{\kappa} + \mathbf{q} - \boldsymbol{\tau}) \right. \\
&\left. + (n_{\text{B}}^j(\mathbf{q}) + 1) \delta(\omega - w_j) \delta(\boldsymbol{\kappa} - \mathbf{q} - \boldsymbol{\tau}) \right],
\end{aligned} \tag{28}$$

$\mathbf{q}$  being the phonon momentum. There are three phonon-polarization vectors  $\boldsymbol{\sigma}^j(\mathbf{q})$  ( $j = 1, 2, 3$ ) with the corresponding phonon energies  $w_j(\mathbf{q})$ . The Bose factor for fixed  $\omega_j$  and  $\mathbf{q}$  is denoted by  $n_{\text{B}}^j(\mathbf{q})$ . The dispersion relation  $w_j = w_j(\mathbf{q})$  can be obtained by solving the lattice dynamics and is often measured in experiments, e.g., by means of neutron scattering. Because of the translational symmetry of the lattice,  $\omega_j$  is a periodic function of  $\mathbf{q}$

$$w_j(\mathbf{q}) = w_j(\mathbf{q} + \boldsymbol{\tau}). \tag{29}$$

Thus, one can restrict values of  $\mathbf{q}$  to the first Brillouin zone ( $\boldsymbol{\tau} = \mathbf{0}$ ) in order to know  $\omega_j$  at any  $\mathbf{q}$ . The dispersion relation for small  $q$  takes the form

$$w_j(\mathbf{q}) = c_s(\boldsymbol{\sigma}^j) q, \tag{30}$$

where  $c_s(\boldsymbol{\sigma}^j)$  is the sound velocity in a given crystal.

The cross section (28) consists of the two terms. The first, which contains the expression  $\delta(\omega + w_j)\delta(\boldsymbol{\kappa} + \mathbf{q} - \boldsymbol{\tau})$  describes annihilation of one phonon. The term with the factor  $\delta(\omega - w_j)\delta(\boldsymbol{\kappa} - \mathbf{q} - \boldsymbol{\tau})$  corresponds to  $a\mu$  scattering with simultaneous one-phonon creation. The annihilation processes vanish when the lattice temperature approaches zero, since there are no phonons at  $T = 0$ . The  $\delta$  functions in Eq. (28) represent conservation of both the energy and momentum, which is a basic feature of the coherent inelastic scattering. By virtue of Eqs. (2) and (28), the initial and final energies and momenta of the muonic atom fulfill the conditions

$$\varepsilon' = \varepsilon + w_j, \quad \mathbf{k}' = \mathbf{k} + \mathbf{q} - \boldsymbol{\tau}, \tag{31}$$

in the case of one-phonon annihilation and obey the conditions

$$\varepsilon' = \varepsilon - w_j, \quad \mathbf{k}' = \mathbf{k} - \mathbf{q} - \boldsymbol{\tau}, \tag{32}$$

when one phonon is created. Therefore, for a fixed scattering angle, only phonons with a specific  $\mathbf{q}$  and  $w_j(\mathbf{q})$  lead to the coherent one-phonon scattering.

It can be shown that the coherent one-phonon creation near the forward direction  $\mathbf{k}' \approx \mathbf{k}$  (possible when  $\boldsymbol{\tau} = \mathbf{0}$ ) takes place only if the velocity of the impinging atom is greater than the sound velocity  $c_s$  [25]. This means that the slowing down of the muonic atom via this process is impossible at the lowest energies.

The isotropic Debye model of a solid is now used for the coherent phonon scattering. The average sound velocity  $c_s$  is substituted in Eq. (30), which is taken as the first approximation to a real-crystal dispersion law. This assumption is reasonable because the coherent phonon processes are important in muonic atom deceleration only at the lowest energies. At higher

energies, incoherent scattering prevails. The factor  $|\boldsymbol{\kappa} \cdot \boldsymbol{\sigma}^j(\mathbf{q})|^2$  in Eq. (28) is replaced by its average value over a surface with a fixed  $w$ . Such an average for the cubic crystals equals  $\kappa^2/3$ , which is a fair approximation even for most noncubic crystals [25]. Using the definition

$$Z(w) \equiv \frac{1}{3N_{\text{mol}}} \sum_{j, \mathbf{q}} \delta[w - w_j(\mathbf{q})] \quad (33)$$

of the normalized density of vibrational states, the summation over  $j$  and  $\mathbf{q}$  in Eq. (28) is replaced by the integration

$$\sum_{j, \mathbf{q}} \longrightarrow 3N_{\text{mol}} \int_0^{w_D} dw Z(w).$$

The result of this integration is then averaged over the directions of  $\boldsymbol{\tau}$  and  $\mathbf{q}$ . Finally, one obtains the following formula:

$$\begin{aligned} \left( \frac{\partial^2 \sigma}{\partial \Omega \partial \varepsilon'} \right)_{\text{coh}, 1}^{\text{inel}} &= N_{\text{mol}} \frac{k'}{k} \sigma_{\text{coh}} \exp(-2W) \frac{\kappa^2}{2M_{\text{mol}}} \\ &\times Z(\omega) \frac{n_B}{(\omega) + 1} \omega \mathcal{R}(\kappa, \omega), \end{aligned} \quad (34)$$

where

$$\begin{aligned} \mathcal{R}(\kappa, \omega) &= \frac{\pi^2}{V_0} \frac{1}{\kappa q} \Theta(w_D - |\omega|) \\ &\times \sum_{\boldsymbol{\tau}} \frac{1}{\tau} \Theta(\tau - |\kappa - q|) \Theta(\kappa + q - \tau) \end{aligned}$$

and  $\Theta$  denotes the Heavyside function. There is a direct relation between this cross section and the incoherent one-phonon cross section

$$\left( \frac{\partial^2 \sigma}{\partial \Omega \partial \varepsilon'} \right)_{\text{coh}, 1}^{\text{inel}} = \frac{\sigma_{\text{coh}}}{\sigma_{\text{inc}}} \mathcal{R}(\kappa, \omega) \left( \frac{\partial^2 \sigma}{\partial \Omega \partial \varepsilon'} \right)_{\text{inc}, 1}. \quad (35)$$

In the limit  $\omega \rightarrow 0$ , the function  $\mathcal{R}$  is proportional to the factor  $\delta(\kappa - \tau)$ . This gives a geometrical condition similar to that for Bragg scattering in a polycrystalline target. Thus, in this limit, the coherent one-phonon scattering displays the same pattern of scattering peaks as that observed in the  $a\mu$ -Bragg-scattering case (apart from  $\tau = 0$ ).

To describe the coherent phonon effects, the function

$$\mathcal{C}_{\text{coh}} \equiv \frac{1}{4\pi N_{\text{mol}}} \left( \frac{M_{a\mu}}{\mathcal{M}} \right)^2 \int d\Omega d\varepsilon' \left( \frac{\partial^2 \sigma}{\partial \Omega \partial \varepsilon'} \right)_{\text{coh}, 1}^{\text{inel}} \quad (36)$$

is defined. A constant  $\mathcal{F}^{\text{mol}}$  is assumed here. In Figs. 5 and 6, both the coherent  $\mathcal{C}_{\text{coh}}$  and incoherent  $\mathcal{C}_{\text{inc}}$  functions are shown in the case of  $p\mu$  scattering in the fcc polycrystalline  $\text{H}_2$  at  $T = 3$  and 13.9 K. The one-phonon coherent and incoherent functions differ strongly below the Bragg-cutoff energy, especially at the lowest temperatures. On the other hand, the total coherent cross sections approach the corresponding incoherent ones at  $\varepsilon$  greater

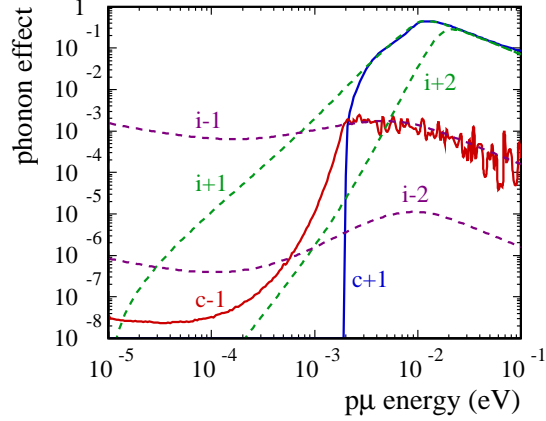


FIG. 5: (Color online) Functions  $\mathcal{C}_{\text{coh}}$  and  $\mathcal{C}_{\text{inc}}$  for  $p\mu$  scattering in the fcc polycrystalline  $\text{H}_2$  at 3 K. Coherent one-phonon annihilation (“c-1”) and creation (“c+1”) are shown using the solid lines. Incoherent (dashed lines) one-phonon processes have the labels: “i-1” (annihilation) and “i+1” (creation). The labels “i-2” and “i+2” stand for the two-phonon incoherent processes.

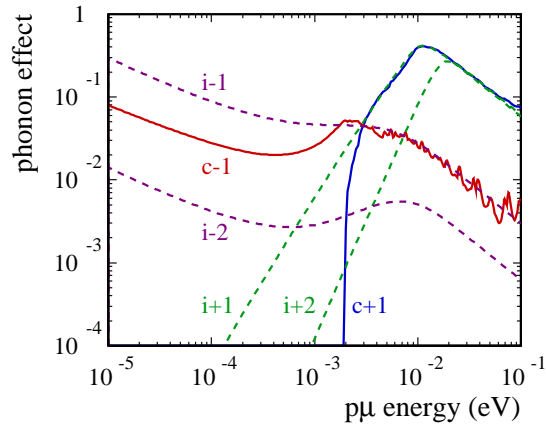


FIG. 6: (Color online) The same as in Fig. 5, for  $T = 13.9$  K.

than a few meV. Since the energy spectrum of a created phonon is broad ( $\approx 9$  meV), the total cross section for one-phonon coherent creation is smooth. Oscillations of the coherent-annihilation cross section apparent at higher energies are due to a narrow width ( $\approx 1$  meV) of the energy spectrum of phonons which exist in the low-temperature targets. The functions  $\mathcal{C}_{\text{inc}}(\varepsilon)$ , which describe the incoherent annihilation and creation of two phonons, are also plotted in Figs. 5 and 6. One can see that the incoherent approximation to multiphonon processes is reasonable because  $\mathcal{C}_{\text{coh}}$  for one-phonon coherent annihilation is much stronger than the correction from two-phonon incoherent annihilation. The only exception can be seen at  $\varepsilon \ll 1$  meV in the 3-K target. However, this energy interval is not important when the slowing down of the  $p\mu$ -atom from  $\varepsilon \sim 1$  eV is considered.

## VI. EXAMPLES OF CROSS SECTIONS FOR HOMOGENEOUS HYDROGENIC TARGETS

Some examples of the cross sections calculated for solid  $\text{H}_2$ ,  $\text{D}_2$ , and  $\text{T}_2$  targets used in the TRIUMF, JINR, and RIKEN-RAL experiments are shown below. They include all the processes which preserve the total spin  $F$  of the muonic atom. In all the cases, the polycrystalline disordered (no specific orientations of molecules in the  $K = 1$  state) fcc structure has been assumed. At temperatures higher than 4 K, the targets can have the polycrystalline hcp structure, which depends on the method of preparation and history of a given target [22, 23]. However, the cross sections for the fcc lattice are good approximations for the hcp structure (apart from the Bragg cross section, which is calculated separately for the hcp case). The reason for this is that the first three shells of neighbor molecules in both lattices are identical if the anisotropic interactions and orientations of molecules are neglected. The molar volumes of both structures are the same. The coherent phonon scattering is important below a few meV, where the acoustic-phonon approximation (30) is valid for the two structures, with practically the same value of the mean sound velocity.

Although the Debye temperatures found in the literature are measured or calculated for crystals that do not exactly correspond to the targets used in muonic-hydrogen physics, these values are taken as a reasonable approximation. The inaccuracy involved by such an approach is estimated to be below 10%. When, for a specific condition, there is no data available, the Debye energy is calculated using the following equation:

$$w_D = 2(3\pi^2)^{1/3} c_s / a_{\text{fcc}}, \quad (37)$$

with the sound velocity  $c_s$  and the lattice constant  $a_{\text{fcc}}$  taken or calculated from Ref. [22].

In Figs. 7–13, the label “total” and the solid lines denote the total cross sections, which include all the coherent and incoherent processes. Contributions to the total cross section from the Bragg scattering (short-dashed line), phonon annihilation (dotted line, label “−phonon”), phonon creation (dash-dotted line, label “+phonon”), and the rotational transition  $K = 1 \rightarrow 0$  (long-dashed line) are also plotted. The lines which describe the phonon processes do not include the rotational-vibrational transitions, although all the incoherent inelastic processes can take place with simultaneous phonon annihilation or creation. Thus, the rotational cross sections shown in these figures also contain the phonon terms. All the presented cross sections are calculated per one hydrogenic molecule bound in the solid target. The cross sections for  $t\mu$  atom scattering in zero-pressure solid  $n\text{T}_2$  at  $T = 3$  and 20 K (just below the melting point) are shown in Figs. 7–10. For the ground state  $F = 0$  of the  $t\mu$  spin, the scattering at the lowest energies is almost fully coherent (a small incoherence is caused by the slightly different single-molecule scattering amplitudes for the two lowest rotational states of  $\text{T}_2$ ). Below the Bragg cutoff, the elastic and phonon-creation coherent processes are forbidden. Thus, in this energy region, the coherent annihilation and incoherent phonon scattering are the only inelastic processes. At the lowest temperatures, however, these processes are strongly suppressed by the Bose factor. As a result, the total cross section in Fig. 7 falls by many orders of magnitude below  $\varepsilon_B$ . This leads to a large increase of the  $a\mu$  mean free path, which results in an enhanced emission of the cold ( $\sim 1$  meV) muonic atoms from the thin solid targets. This phenomenon has been already observed in the TRIUMF experiment [5], in the case of  $p\mu$  atoms. When the target temperature is raised, the low-energy phonon processes become more important and, near the melting temperature, the phonon cross section is quite large at  $\varepsilon \rightarrow 0$  (see Fig. 8).

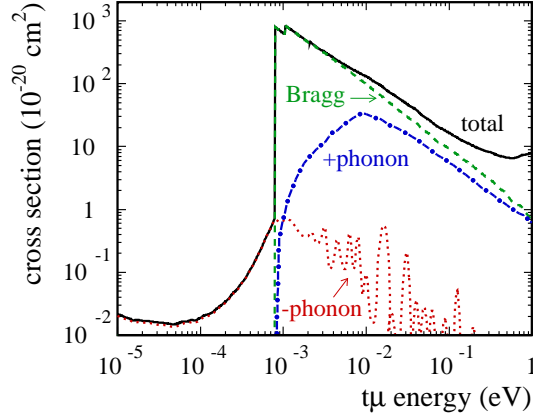


FIG. 7: (Color online) Total cross section for  $t\mu(F = 0)$  scattering in zero-pressure solid  $nT_2$  at  $T = 3$  K. Contributions from Bragg scattering, phonon creation (+phonon), and phonon annihilation (-phonon) processes are also shown.

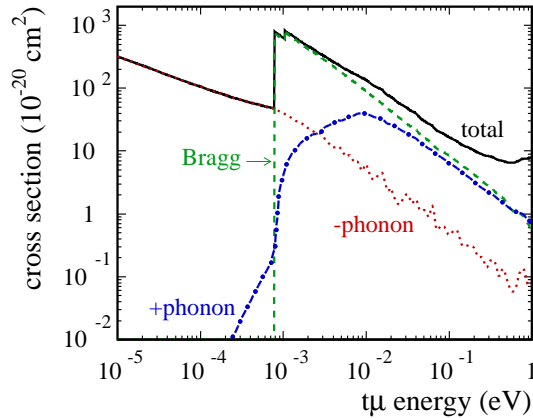


FIG. 8: (Color online) The same as in Fig. 7 for  $t\mu(F = 0)$  and  $T = 20$  K.

For  $F = 1$ , both the coherent and incoherent processes are significant since  $\sigma_{\text{inc}}$  is appreciable (cf. Table I). Therefore, the total cross section below  $\varepsilon_B$  does not fall so greatly, compared to the  $F = 0$  case. The other important difference between the  $F = 0$  and  $F = 1$  cases is the rotational deexcitation  $K = 1 \rightarrow 0$ , which is due to the muon exchange between the tritium nuclei with the opposite spin projections. At the lowest energies, such a transition leads to an effective acceleration of the muonic atom. This transition is forbidden when the total spin of  $t\mu(F = 0)$  is conserved in the collision process. On the other hand, such a transition can take place with the simultaneous excitation  $F = 0 \rightarrow 1$  of the  $t\mu$  spin state. However, the spin-flip process has a threshold of 0.237 eV (in the  $t\mu + t$  center of mass) so that this reaction cannot occur at the lowest energies.

Similar features of the cross sections appear in the  $p\mu$  atom scattering in zero-pressure solid  $nH_2$ . Figures 11 and 12 show the cross sections for  $F = 0$  and  $F = 1$  at  $T = 13.9$  K (below the melting temperature of the solid  $H_2$ ). The analogous cross sections for  $T = 3$  K were presented in Ref. [5, 20]. For  $p\mu(F = 1)$ , the incoherent scattering at the lowest energies



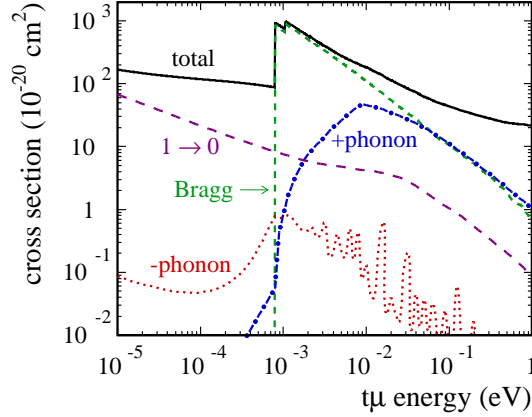


FIG. 9: (Color online) The same as in Fig. 7 for  $t\mu(F = 1)$  and  $T = 3$  K. The label “ $1 \rightarrow 0$ ” denotes the rotational deexcitation  $K = 1 \rightarrow 0$  of the target molecule.

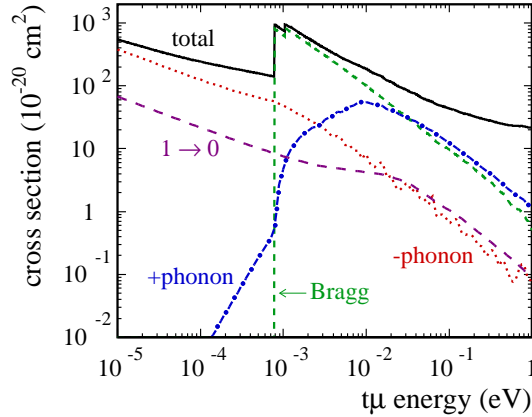


FIG. 10: (Color online) The same as in Fig. 9 for  $t\mu(F = 1)$  and  $T = 20$  K.

is more pronounced than in the tritium case since  $\sigma_{\text{inc}}$  is comparable to  $\sigma_{\text{coh}}$  (cf. Table I).

In the deuterium case,  $d\mu$  atom scattering from the  $\text{D}_2$  molecule does not significantly depend on the  $d\mu$ -atom total spin [18]. Therefore, the cross sections for  $d\mu(F = 1/2)$  and  $d\mu(F = 3/2)$  scattering in solid  $\text{D}_2$  are very similar. The rotational deexcitation  $K = 1 \rightarrow 0$  of the target molecule in  $d\mu$  scattering which conserves the total spin  $F$  is allowed for both the  $F = 1/2$  and  $F = 3/2$  states. In Fig. 13, the total cross section for  $d\mu(F = 1/2)$  scattering in zero-pressure  $n\text{D}_2$  is plotted for the target temperature just below the melting point. For the ortho- $\text{D}_2$  target, there is no rotational deexcitation. Thus, in this case, the phonon annihilation is the only  $d\mu$ -acceleration process, which is shown in Fig. 14 for  $T = 3$  K.

In Fig. 15, the total cross sections for  $d\mu$  and  $t\mu$  scattering in 3-K solid  $n\text{H}_2$  are plotted. They can also be applied for solid  $\text{H}_2$  with a very small admixture of  $\text{D}_2$  or  $\text{T}_2$ . When a  $\mu^-$  beam is stopped in such a target, it is mainly  $p\mu$  atoms which are created. Some of them can then hit a  $\text{D}_2$  or a  $\text{T}_2$  molecule, which mostly leads to the isotopic muon transfer [31]. As a result, the released  $d\mu$  or  $t\mu$  atom has a kinetic energy on the order of a few tens eV. During the deceleration process, these atoms are emitted to vacuum while they reach the Ramsauer-

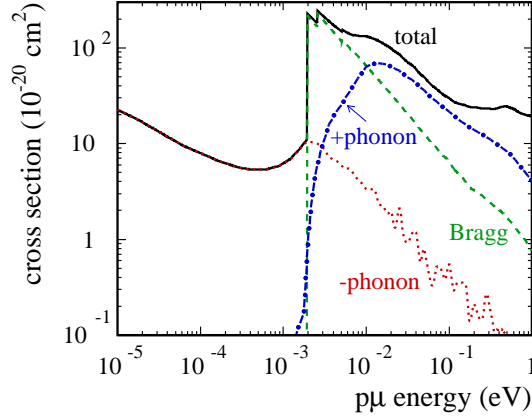


FIG. 11: (Color online) Total cross section for  $p\mu(F = 0)$  scattering in zero-pressure solid  $n\text{H}_2$  at  $T = 13.9$  K. The notation is the same as in Fig. 7.

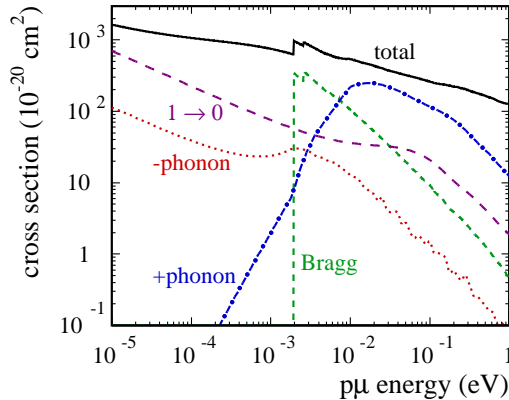


FIG. 12: (Color online) Total cross section for  $p\mu(F = 1)$  scattering in zero-pressure solid  $n\text{H}_2$  for  $F = 0$  at  $T = 13.9$  K. The notation is the same as in Fig. 9.

Townsend minima, which is apparent at about 10 eV. This mechanism has been used for the production of the energetic (1-10 eV)  $d\mu$  and  $t\mu$  beams at TRIUMF [1, 2, 3, 4, 5, 6]. The calculated differential cross sections establish the basis for accurate simulations of the emission of such muonic-atom beams. Fig. 15 shows also that one should expect an enhanced emission of the cold ( $\sim 1$ -meV) muonic atoms from the target, due to the falloff of the total cross sections below the Bragg cutoff.

## VII. MUONIC ATOM DECELERATION IN HYDROGENIC CRYSTALS

When a  $\mu^-$  beam is stopped in a hydrogenic target, the muonic hydrogen atoms are created in the highly excited Coulombic states. During the deexcitation process, these atoms gain kinetic energy. As a result, the ground-state 1S atoms have a broad energy distribution (see e.g., Refs. [32, 33, 34, 35, 36]), which can even extend to  $10^3$  eV. Since the muonic atomic and muonic-molecular processes strongly depend on the  $a\mu$  energy, it is necessary to know its time evolution. In the solid targets, the  $a\mu$  deceleration from the highest energies

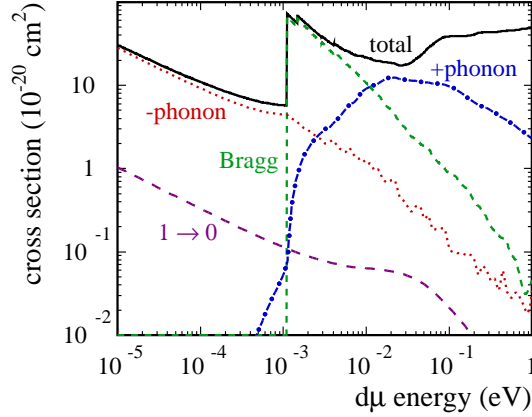


FIG. 13: (Color online) Total cross section for  $d\mu(1/2)$  scattering in zero-pressure solid  $nD_2$  at  $T = 18.7$  K. The notation is the same as in Fig. 9.

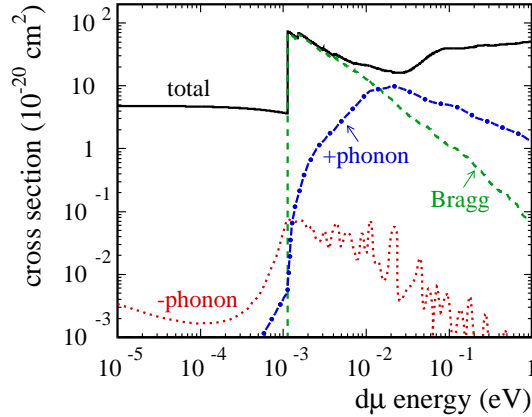


FIG. 14: (Color online) Total cross section for  $d\mu(3/2)$  scattering in zero-pressure solid ortho- $D_2$  at  $T = 3$  K. The notation is the same as in Fig. 7.

to about 0.1 eV is very fast ( $\sim 1$  ns). Therefore, only the last stage of  $a\mu$  slowing down, when solid-state effects are important, is considered here. The Maxwell distribution of the initial  $a\mu$  kinetic energy with the mean value  $\varepsilon_{\text{avg}} = 1$  eV and the statistical population of the initial  $a\mu$  spin states are assumed. The mean energy  $\varepsilon_{\text{avg}}$  as a function of time and temperature has been evaluated using the calculated differential cross sections and Monte Carlo simulations.

In Figs. 16–17,  $\varepsilon_{\text{avg}}$  for the  $p\mu$  atom in solid  $nH_2$  and for the  $t\mu$  atom in solid  $nT_2$  is plotted versus time. This energy is additionally averaged over the muonic-atom spin  $F$ . In fact, after about 1 ns, the higher spin states  $F = 1$  of the  $p\mu$  and  $t\mu$  atoms are depleted because of the large downwards spin-flip cross section [16]. The deceleration of  $p\mu$ 's to  $\varepsilon_{\text{avg}} = 10$  meV is very fast. This stage is much longer for  $t\mu$ 's as the cross section  $t\mu(F = 0) + t$  is relatively small at the lowest energies [17]. Below 10 meV, solid-state effects are very important and, therefore, they strongly affect the slowing down. This is especially visible at 3 K, when the phonon processes are suppressed and the classical thermal energy  $3k_B T/2$  is much smaller than the Bragg cutoff energy  $\varepsilon_B$  (see Fig. 7). Below  $\varepsilon_B$ , there is no effective deceleration

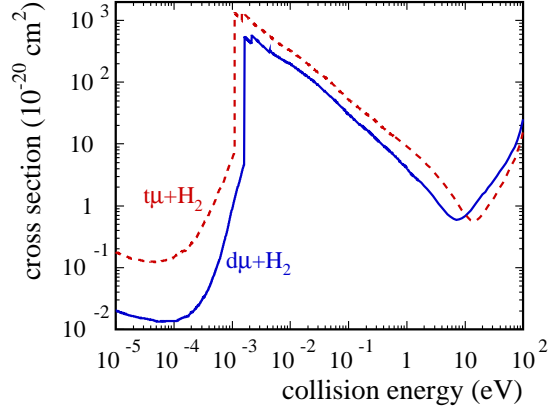


FIG. 15: (Color online) Total cross sections for  $d\mu$  and  $t\mu$  scattering in 3-K solid  $n\text{H}_2$ .

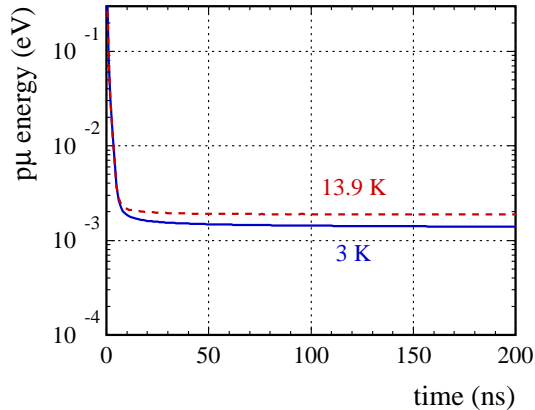


FIG. 16: (Color online) Mean energy of a  $p\mu$  atom in solid  $n\text{H}_2$  versus time at  $T = 3$  and 13.9 K.

mechanism. As a result, at the lowest temperatures, the mean energy of the muonic atoms in the steady state is much higher than the thermal energy. This energy is achieved after about 200 ns. The deceleration below 10 meV is slow since the scattering is dominated by the elastic Bragg process. On the other hand, when the target temperature tends to the melting point,  $3k_{\text{B}}T/2$  is greater than  $\varepsilon_{\text{B}}$  and the deceleration is faster. Also, the steady-state  $\varepsilon_{\text{avg}}$  already approaches  $\mathcal{E}_T$  (cf. the cross sections from Figs. 8 and 11). One sees that the difference between the steady-state values of  $\varepsilon_{\text{avg}}$  is much smaller than the difference of the corresponding classical thermal energies for the two limiting temperatures. This is especially pronounced in solid  $\text{H}_2$ , where  $\varepsilon_{\text{B}}$  is the greatest and the melting temperature is the smallest, compared to the solid  $\text{D}_2$  and  $\text{T}_2$  targets. The analogous deceleration functions for  $d\mu$  atom in solid  $n\text{D}_2$  are plotted in Fig. 18. Since the spin-flip rate for this case is very small [16], the deexcitation of the upper spin state is completed only after about 100 ns. This additionally extends the slowing down process as the hyperfine-splitting energy of 48.5 meV is released.

In Fig. 19, the dependence of  $\varepsilon_{\text{avg}}$  in the steady state is shown as a function of the target temperature, for the solid  $n\text{D}_2$  and  $n\text{T}_2$  targets. A full set of the differential cross sections has been calculated for about ten values of the temperature. Then, the mean energy has

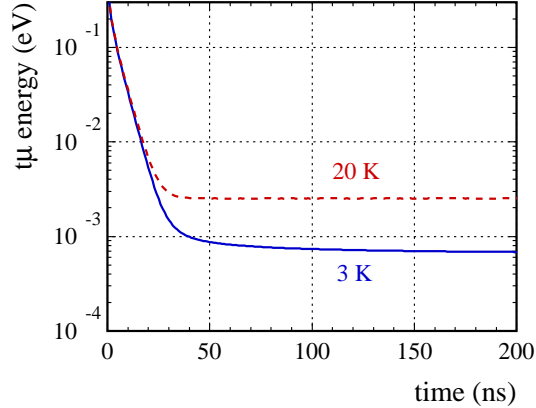


FIG. 17: (Color online) Mean energy of a  $t\mu$  atom in solid  $nT_2$  versus time at  $T = 3$  and 20 K.

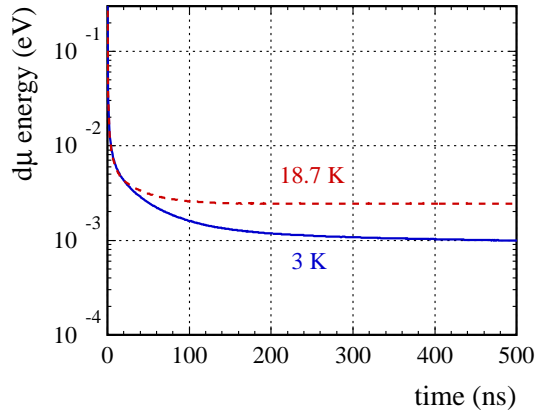


FIG. 18: (Color online) Mean energy of a  $d\mu$  atom in solid  $nD_2$  versus time at  $T = 3$  and 18.7 K.

been estimated by means of Monte-Carlo simulations. Below a few Kelvin,  $\varepsilon_{\text{avg}}$  is almost constant, which is due to the lack of effective deceleration mechanisms at  $\varepsilon \lesssim 1$  meV. At higher temperatures,  $\varepsilon_{\text{avg}}$  changes almost linearly and approaches  $3k_B T/2$  near the melting point.

## VIII. CONCLUSIONS

The differential cross sections for muonic hydrogen atom scattering in the polycrystalline hydrogenic targets have been calculated using the scattering amplitudes for single molecules and the response function for the isotropic solid. A certain number of important approximations has been made in the presented calculations. The scattering amplitudes for isolated hydrogenic molecules are obtained using the corresponding amplitudes for muonic atom scattering from free hydrogen-isotope nuclei [16, 17] and the first-Born approximation. It is assumed that the molecular vibrations are harmonic and that there is no coupling between the vibrational and rotational degrees of freedom. The presence of electrons in the target molecules is taken into account by introduction of the effective electron-screening potential.

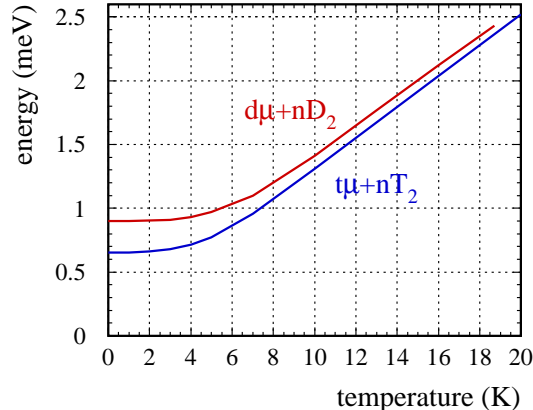


FIG. 19: (Color online) The calculated mean energy of a  $d\mu$  atom in solid  $nD_2$  and of a  $t\mu$  atom in solid  $nT_2$  at large times versus the target temperature.

These approximations have been discussed in detail in Ref. [19]. In the case of solid molecular targets, it is assumed that the rotational-vibrational structure of the bound molecules is not changed, which is a fair approximation for the low-pressure hydrogenic crystals [22, 23]. These targets are described in the harmonic approximation and the response function for the isotropic Debye solid is used. The Debye model is applied for estimation of the coherent and incoherent phonon cross sections. Coherent and incoherent effects are separately taken into account only in the most important one-phonon scattering. The cross sections for multiphonon processes are calculated in the incoherent approach.

It happens that the muonic atom coherent scattering is very important in the  $H_2$ ,  $D_2$ , and  $T_2$  targets at  $\varepsilon \lesssim 10$  meV. In particular, a rapid decrease of the total cross section below the Bragg cutoff energy leads to an enhanced emission of cold muonic atoms at temperatures  $T \lesssim 5$  K, where the phonon annihilation processes are strongly suppressed. The enhanced emission of  $p\mu$  atoms has been observed and is well described by the calculated differential cross sections [5]. The coherent phonon creation disappears below about 2 meV. Since this process is the only mechanism of deceleration at the lowest energies, the mean energy of muonic atoms at  $T \lesssim 5$  K is much greater than the corresponding energy in a perfect-gas target. Also, the deceleration process below 10 meV becomes much slower at such temperatures, since the elastic Bragg scattering in a heavy target cannot change the kinetic energy of the muonic atoms.

Above about 10 meV, the rotational and then vibrational excitations of the target molecules support a very effective mechanism for the deceleration of muonic atom. At  $\varepsilon \gtrsim 100$  meV, the cross sections for the hydrogenic crystals (per one molecule) tend to those calculated for the isolated hydrogenic molecules. However, the effective temperature of molecules in the hydrogenic crystals is much higher than the target temperature, due to the zero-point vibrations of the molecules in the lattice. This effect does not disappear (even at high collision energies).

Although coherent and incoherent phonon effects have been estimated in the simplest approach of the isotropic Debye solid, the Monte Carlo simulations using the calculated

differential cross sections are in good agreement with the available experimental data.

---

- [1] P. E. Knowles et al., Phys. Rev. A **56**, 1970 (1997).
- [2] M. C. Fujiwara et al., Phys. Rev. Lett. **85**, 1642 (2000).
- [3] T. A. Porcelli et al., Phys. Rev. Lett. **86**, 3763 (2001).
- [4] G. M. Marshall et al., Hyperfine Interact. **138**, 203 (2001).
- [5] J. Woźniak et al., Phys. Rev. A **68**, 062502 (2003).
- [6] F. Mulhauser et al., Phys. Rev. A **73**, 034501 (2006).
- [7] D. L. Demin et al., Hyperfine Interact. **101/102**, 13 (1996).
- [8] C. Petitjean, Hyperfine Interact. **138**, 191 (2001).
- [9] T. Matsuzaki et al., Phys. Lett. B **557**, 176 (2003).
- [10] A. Toyoda et al., Phys. Rev. Lett. **90**, 243401 (2003).
- [11] N. Kawamura et al., Phys. Rev. Lett. **90**, 043401 (2003).
- [12] K. Ishida et al., Nucl. Phys. B-Proc. Sup. **149**, 351 (2005).
- [13] H. Imao et al., Phys. Lett. B **632**, 192 (2006).
- [14] P. Strasser et al., Nucl. Phys. A **746**, 621 (2004).
- [15] P. Strasser et al., Nucl. Phys. B-Proc. Sup. **149**, 390 (2005).
- [16] L. Bracci et al., Phys. Lett. A **134**, 435 (1989).
- [17] L. Bracci et al., Phys. Lett. A **149**, 463 (1990).
- [18] A. Adamczak et al., At. Data Nucl. Data Tables **62**, 255 (1996).
- [19] A. Adamczak, Phys. Rev. A **74**, 042718 (2006).
- [20] A. Adamczak, Hyperfine Interact. **119**, 23 (1999).
- [21] L. Van Hove, Phys. Rev. **95**, 249 (1954).
- [22] P. C. Souers, *Hydrogen Properties for Fusion Energy* (University of California Press, Berkeley, 1986).
- [23] I. F. Silvera, Rev. Mod. Phys. **52**, 393 (1980), and references therein.
- [24] J. Van Kranendonk, *Solid Hydrogen* (Plenum Press, New York and London, 1983).
- [25] S. W. Lovesey, *Theory of Neutron Scattering from Condensed Matter* (Clarendon Press, Oxford, 1984).
- [26] K. S. Singwi and A. Sjölander, Phys. Rev. **120**, 1093 (1960).
- [27] G. H. Vineyard, Phys. Rev. **110**, 999 (1958).
- [28] K. W. Herwig et al., Phys. Rev. B **41**, 96 (1990).
- [29] F. J. Mompeán et al., Phys. Rev. B **54**, 970 (1996).
- [30] M. Zoppi, D. Colognesi, and M. Celli, Eur. Phys. J. B **23**, 171 (2001).
- [31] A. Adamczak et al., Phys. Lett. B **285**, 319 (1992).
- [32] V. E. Markushin, Phys. Rev. A **50**, 1137 (1994).
- [33] D. J. Abbott et al., Phys. Rev. A **55**, 214 (1997).
- [34] M. P. Faifman and L. I. Menshikov, Hyperfine Interact. **138**, 61 (2001).
- [35] T. S. Jensen and V. E. Markushin, Eur. Phys. J. D **21**, 271 (2002).
- [36] R. Pohl et al., Phys. Rev. Lett. **97**, 193402 (2006).